AIDA

Advanced European Infrastructures for Detectors at Accelerators

Journal Publication

Performance of fully instrumented detector planes of the forward calorimeter of a Linear Collider detector

Abramowicz, H (TAU) *et al*

17 November 2014

The electronic version of this AIDA Publication is available via the AIDA web site <http://cern.ch/aida> or on the CERN Document Server at the following URL: <http://cds.cern.ch/search?p=AIDA-PUB-2014-029>

arXiv:1411.4431v1 [physics.ins-det] 17 Nov 2014

Performance of fully instrumented detector planes of the forward calorimeter of a Linear Collider detector

The FCAL collaboration
November 15, 2014

H. Abramowicz[a], A. Abusleme[b], K. Afanaciev[c], J. Aguilar[d,1] E. Alvarez[b], D. Avila[b],
Y. Benhammou[a], L. Bortko[e,2], O. Borysov[a], M. Bergholz[e,2] I. Bozovic-Jelisavcic[f],
E. Castro[e,3] C. Coca[g], W. Daniluk[d], L. Dumitru[g], K. Elsener[h], V. Fadeyev[i], M. Firlej[j],
E. Firu[k], T. Fiutowski[j], V. Ghenescu[k], H. Henschel[e], M. Idzik[j], A. Ishikawa[l],
S. Kananov[a], S. Kollowa[e,4] J. Kotula[d], B. Krupa[d], Sz. Kulis[j,5] W. Lange[e], T. Lesiak[d],
A. Levy[a], I. Levy[a], W. Lohmann[e,2] S. Lukic[f], C. Milke[i], J. Moron[j], A. Moszczynski[d],
A.T. Neagu[k], O. Novgorodova[e,6] M. Orlandea[g], K. Oliwa[d], M. Pandurovic[f], B. Pawlik[d],
T. Preda[k], D. Przyborowski[j], O. Rosenblat[a], A. Sailer[h], Y. Sato[l,7] B. Schumm[i],
S. Schuwalow[e,8] I. Smiljanic[f], K. Swientek[j], E. Teodorescu[g,9] P. Terlecki[j],
W. Wierba[d], T. Wojton[d], S. Yamaguchi[l], H. Yamamoto[l], L. Zawiejski[d], I.S. Zgura[k]

[a]*Tel Aviv University, Tel Aviv, Israel*
[b]*Pontificia Universidad Catolica de Chile, Santiago, Chile*
[c] *NC PHEP, Belarusian State University, Minsk, Belarus*
[d]*INP PAN, Cracow, Poland*
[e]*DESY, Zeuthen, Germany*
[f]*Vinca Institute of Nuclear Sciences, University of Belgrade, Serbia*
[g]*INFIN-HH, Bucharest, Romania*
[h]*CERN, Geneva, Switzerland*
[i]*University of California, Santa Cruz, USA*
[j]*AGH University of Science and Technology, Cracow, Poland*
[k]*ISS, Bucharest, Romania*
[l] *Tohoku University, Sendai, Japan*

E-mail: levyaron@post.tau.ac.il

ABSTRACT: Detector-plane prototypes of the very forward calorimetry of a future detector at an e^+e^- collider have been built and their performance was measured in an electron beam. The detector plane comprises silicon or GaAs pad sensors, dedicated front-end and ADC ASICs, and an FPGA for data concentration. Measurements of the signal-to-noise ratio for different feedback schemes and the response as a function of the position of the sensor are presented. A deconvolution method is successfully applied, and a comparison of the measured shower shape as a function of the absorber depth with a Monte-Carlo simulation is given.

KEYWORDS: very-forward calorimetry, sampling calorimeter, luminosity, ILC, CLIC, linear collider.

[1] Now at John Hopkins University, Baltimore, USA

[2] Also at Brandenburg University of Technology, Cottbus, Germany

[3] Now at DESY, Hamburg, Germany

[4] Now at Institute fuer Kristallzeuchtung, Berlin,Germany

[5] Now at CERN, Geneva, Switzerland

[6] Now at Technical University Dresden, Dreseden, Germany

[7] Now at Nagoya University, Nagoya, Japan

[8] Also at University of Hamburg, Hamburg, Germany

[9] Now at National Institute for Laser, Plasma and Radiation Physics(INFLPR), Bucharest-Magurele, Romania

Contents

1. Introduction

Future e^+e^- colliders offer a rich experimental program that addresses many open issues in elementary particle physics. For example, the recent discovery of a Higgs boson [1] challenges to fully exploit the mechanism of Spontanuous Symmetry Breaking. For the moment, two such colliders, distinguished by their acceleration concepts and by their energy reach, are being studied; the International Linear Collider (ILC) [2], based on superconducting cavities, and the Compact Linear Collider (CLIC) [3] with the two-beam concept. For the ILC, two types of detectors are under design, the International Large Detector (ILD) [4] and the Silicon Detector (SiD) [5]. Similar concepts are also worked out for CLIC, CLIC_ILD and CLIC_SiD [3, 6]. For the luminosity determination, a system of very forward detectors is designed, which can be adapted to any of the detectors at future linear colliders.

Two special calorimeters [7] are foreseen in the very forward region of a future detector, the Luminosity Calorimeter (LumiCal) and the Beam Calorimeter (BeamCal). The LumiCal will measure the luminosity with a precision of better than 10^{-3} at 500 GeV centre-of-mass energy and 3×10^{-3} at 1 TeV centre-of-mass energy at the ILC, and with a precision of 10^{-2} at CLIC. The BeamCal will perform a bunch-by-bunch estimate of the luminosity and, supplemented by a pair monitor, assist beam tuning when included in a fast feedback system [8]. Both calorimeters extend
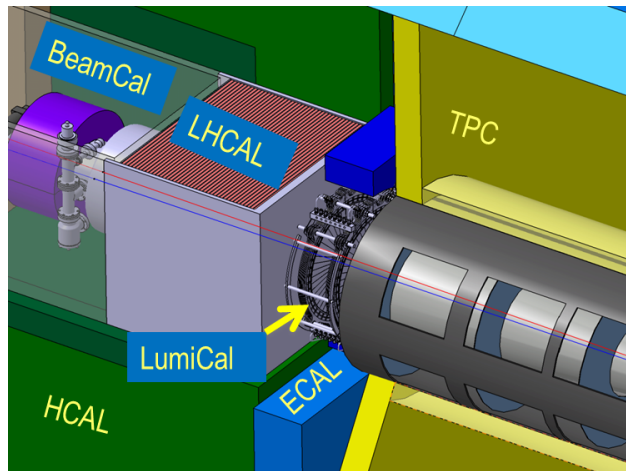

Figure 1: The very forward region of the ILD detector. LumiCal, BeamCal and LHCAL are carried by the support tube for the final focusing quadrupole QD0 and the beam-pipe. TPC denotes the central tracking chamber, ECAL the electromagnetic and HCAL the hadron calorimeter.

the detector coverage to low polar angles, important e.g. for new particle searches with a missing energy signature [9]. A sketch of the design is shown in Figure 1 for the ILD detector. The LumiCal is positioned in a circular hole of the end-cap electromagnetic calorimeter ECAL. The BeamCal is placed just in front of the final focus quadrupole. LumiCal covers polar angles between 31 and 77 mrad and BeamCal, between 5 and 40 mrad.

Both calorimeters consist of 3.5 mm-thick tungsten absorber disks, each corresponding to around one radiation length, interspersed with sensor layers. Each sensor layer is segmented radially and azimuthally into pads. The read-out rate is driven by the beam-induced background. Due

to the high occupancy originating from beamstrahlung and two-photon processes, both calorime-ters need a fast readout. Front-end (FE) and ADC ASICs are placed at the outer radius of the calorimeters. In addition, the lower polar-angle range of BeamCal is exposed to a large flux of low energy electrons, resulting in depositions up to one MGy for a total integrated luminosity of 500 fb^{-1} at 500 GeV. Hence, radiation hard sensors are needed.

Prototype detector planes assembled with FE- and ADC-ASICs for LumiCal and for BeamCal have been built. In this paper, results of their performance following tests in an electron beam are reported.

2. Prototype detector planes

The detector planes consist of silicon or gallium arsenide (GaAs) pad sensors instrumented with FE and ADC ASICs. The sensors are sufficiently fast to be used for both the ILC and the CLIC colliders. The current FE electronics is designed for the ILC.

2.1 Silicon sensors

Prototypes of LumiCal silicon sensors have been designed at the Institute of Nuclear Physics PAN in Cracow [10] and manufactured by Hamamatsu Photonics. A picture of a sensor is shown in Figure 2.
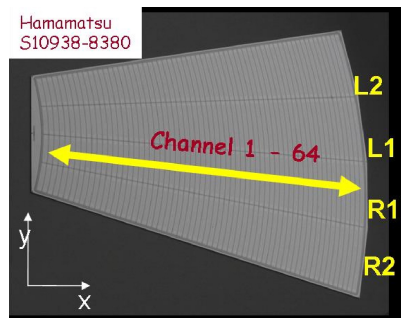

Figure 2: A prototype silicon sensor for LumiCal

Its shape is a ring segment of 30° and it contains four sectors, 7.5° each. The thickness of the n-type silicon bulk is 320 μm. The pitch of the concentric p$^+$ pads is 1.8 mm and the gap between two pads is 100 μm. All sensors were characterised in the laboratory for their electrical qualities. The capacitance as a function of the bias voltage for different pads is shown in Figure 3(a). The leakage current of the same pads is shown in Figure 3(b). The bias voltage for full depletion ranges between 35 and 60 V and the leakage currents per pad are below 6 nA. Pad capacitances between 10 pF (L2 Ch2), for the smallest pads, and 25 pF, for the largest pads (L2 Ch64), were measured [10, 11]. The pad capacitance measurements as a function of the bias voltage also show that the sensor resistivity is of the order of 0.7×10^6 Ωm [10].

2.2 GaAs sensors

The BeamCal prototype sensors have been produced by Tomsk State University. The sensors were produced using the liquid encapsulated Czochralski method and were doped with Sn, as a shallow
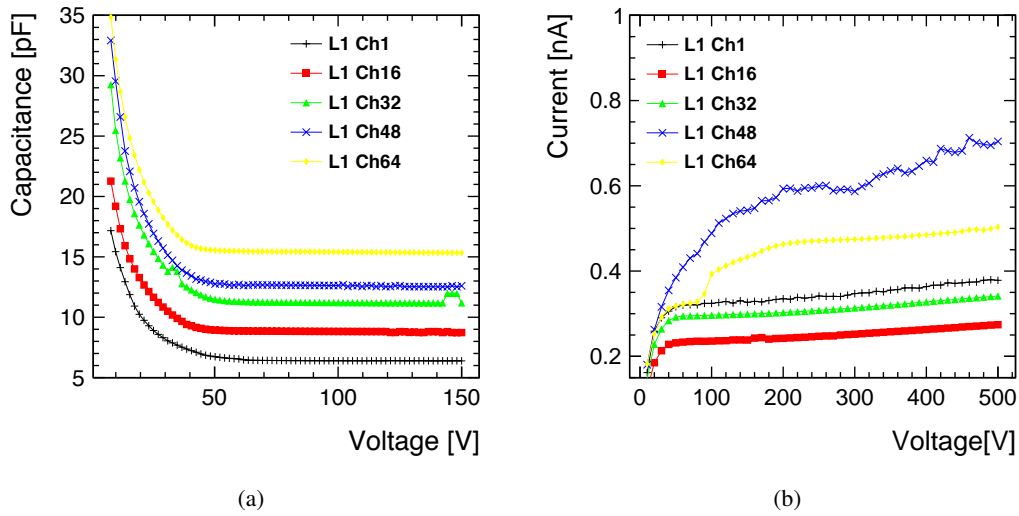
Figure 3: (a) The dependence of the capacitance on the bias voltage for different pads of a silicon sensor. (b) The leakage-current dependence on the bias voltage, for the same pads.

donor, and compensated with chromium, as a deep acceptor. This results in a semi-insulating GaAs material with a resistivity of about 10^7 Ωm. It should be noted that, due to the properties of the compensated material, the hole lifetime is very low and the signal is predominantly generated by electron drift. As a consequence, the maximum reachable charge-collection efficiency of the GaAs sensor is 50% for particles fully crossing the sensor. The GaAs sensor has a thickness of 500 μm. Its shape is a ring segment of 22.5°. The inner radius is 48 mm and the outer one, 114 mm. It is metallised with 1 μm of Ni on both sides. One side has a solid metallisation and the opposite side is segmented into 12 rings and each ring into pads with different area depending on the radius, as shown in Figure 4. The total number of pads is 64. The minimal pad area is 18 mm^2 and the
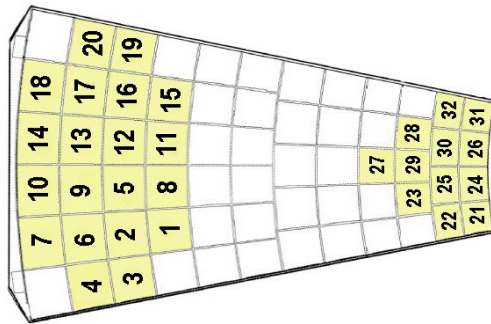

Figure 4: Prototype of a GaAs sensor. Each pad is identified by a number.

maximal pad area is 42 mm^2. The gap between two pads is 200 μm.

Before the beam-test, the sensors were characterised in the laboratory. The charge-collection efficiency (CCE) and the leakage current were measured as a function of the applied voltage and are shown in Figure 5 and Figure 6, respectively, for several pads. The CCE saturates at 50% at

field strength of 0.2 V/μm for all pads. Pad capacitances vary between 5 pF for the smallest pads and 12 pF for the largest pads. Previously, a study was done to determine the radiation hardness of the compensated GaAs sensors in a 10 MeV electron beam [12]. The charge-collection efficiency was measured during irradiation. It drops by a factor of 10, but a signal from a minimum ionising particle is still visible after an absorbed dose of 1.5 MGy. The leakage current of a pad before irradiation was about 0.4 μA. After exposure to a dose of 1.5 MGy, the leakage current increased to about 1 μA at an electric-field strength of 0.4 V/μm.
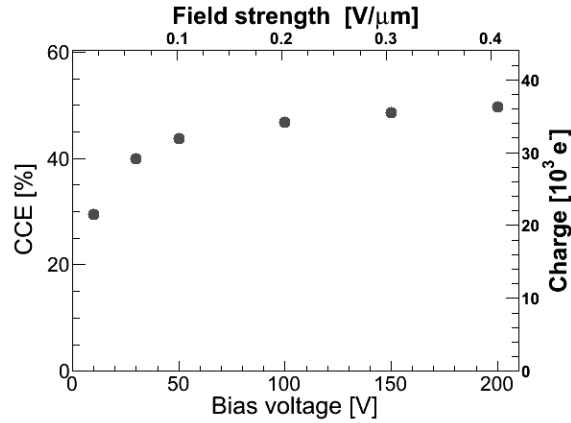
Figure 5: Charge-collection efficiency (CCE) and the charged measured as a function of the applied voltage for different pads of the GaAs sensor.
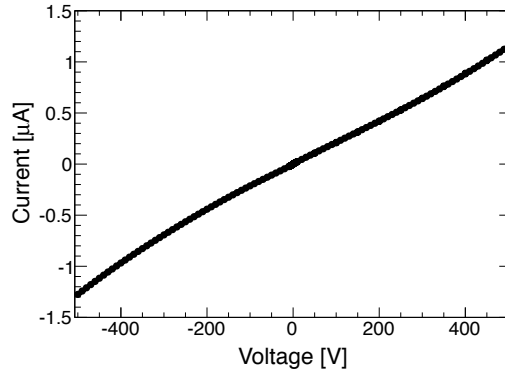
Figure 6: The leakage current as a function of the applied voltage for pad 5 in ring 5.

2.3 Detector planes

Thin printed circuit boards (PCBs) with copper traces were used as fan-outs. They were glued to sensors. The fan-out itself was screwed to an additional PCB carriage with a window corresponding

to the sensor shape. Fan-out traces at one end were bonded to a connector to the read-out electronics board and at the other end to the pads through small holes. High voltage was applied to the fully metalised side of the sensor. Finally, the fully assembled prototypes were put into a light-tight shielding box.

3. Readout electronics

The readout electronics were developed according to the specifications imposed by operating conditions and constraints [13]. The frond-end circuits were designed to work in two modes: the physics mode and the calibration mode. In the physics mode (low gain) the detector should be sensitive to electromagnetic showers resulting in high energy deposition and the front-end electronics should process signals up to almost 10 pC per channel. In the calibration mode (high gain) it should detect signals from relativistic muons, hereafter referred to as minimum ionizing particles (MIPs) to be used for calibration and alignment. The proposed sensor geometry results in a capacitive load (sensor and fanout) between 5 pF - 35 pF connected to a single front-end channel. Because of high expected occupancy per channel, the front-end should be fast enough to process signals from subsequent beam bunches which, for the ILC, are separated in time by about 350 ns. The simulations of LumiCal and BeamCal indicate that the shower reconstruction needs a 10-bit Analog-to-Digital Converter (ADC). Severe requirements on the power dissipation of readout electronics may be strongly relaxed if the power is switched off between bunch trains. This is feasible for the ILC, since a 200 ms pause is foreseen after each 1 ms long bunch train [14].
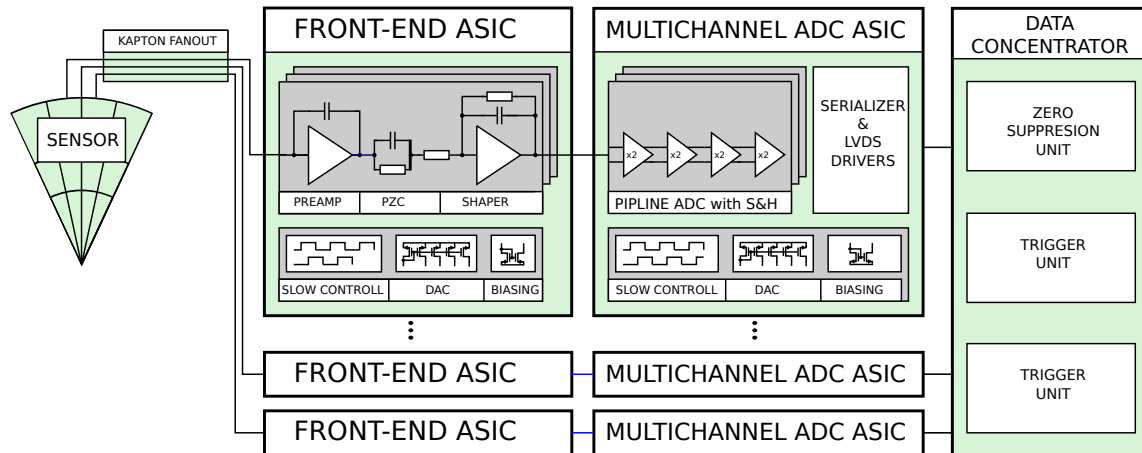

Figure 7: Block diagram of the LumiCal readout-chain.

From the above specifications, a general concept of the readout chain, comprising dedicated readout ASICs, was outlined, as shown in Figure 7. The main blocks of the signal-processing chain are sensor, FE-electronics ASIC, ADC-ASIC and Field Programmable Gate Array (FPGA) based data concentrator.

3.1 Front-end electronics

To fulfill the above requirements, the front-end architecture comprising a charge sensitive amplifier, a pole-zero cancellation circuit (PZC) and a shaper was chosen [15], as shown in Figure 8. In order

to cope with large input charges in the physics mode and the small ones in the calibration mode, a variable gain in the charge amplifier and shaper was implemented. The "mode" switch in Figure 8 changes effective values of the feedback circuit components R_f, C_f, R_i, C_i and so changes the transimpedance gain of the front-end. In the preamplifier feedback and the PZC two versions of resistance were implemented; a standard passive resistance, henceforth referred to as R_f feedback, and a MOS transistor working in a linear region, henceforth referred to as *MOS* feedback. In addition, for the calibration mode, the preamplifier gain in the *MOS* feedback version was set two times higher than in the R_f feedback version. Setting the PZC parameters properly ($C_f R_f = C_p R_p$) and equalizing shaping time constants ($C_i R_i = C_p(R_p||R_s)$) one obtains the first-order shaping, equivalent to a CR-RC filter, with a peaking time $T_{peak} = C_i R_i$, which was set close to 60 ns.
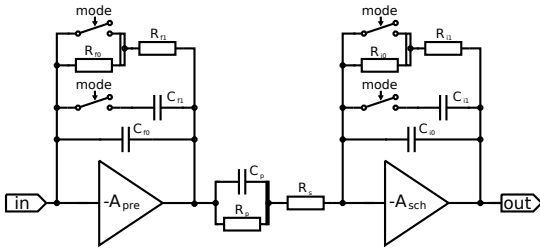

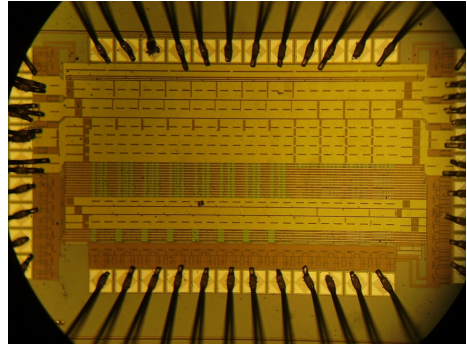Figure 8: Block diagram of a front-end channel.

Figure 9: Micrograph of a front-end ASIC.

The prototype ASIC, containing 8 front-end channels (4 with R_f feedback, 4 with *MOS* feedback), was designed and fabricated in 0.35 μm four-metal two-poly CMOS technology. The area occupied by a single channel is 630 μm $\times$ 100 μm. The photograph of the prototype glued and bonded on the PCB is shown in Figure 9. Systematic measurements of the essential parameters like gain, noise, high count-rate performance and crosstalk, were performed and described in detail in [15], confirming the expectations.

3.2 Multichannel ADC

To apply an analog-to-digital conversion in each front-end channel, a dedicated low power, small area, multichannel ADC is needed. For an ILC detector, a sampling rate of about 3 MS/s will be sufficient while for the beam-test purpose a much faster ADC, allowing few samples per pulse, is beneficial. To meet both requirements, a general purpose variable-sampling-rate ADC with scalable power consumption was developed.

The block diagram of the designed multichannel digitiser ASIC [16] is shown in Figure 10. It comprises eight 10-bit ADCs with variable power and sampling frequency (up to 24 MS/s), a configurable digital serializer circuit, fast variable power Low Voltage Differential Signaling (LVDS) I/O circuits, a set of Digital-to-Analog converters for automatic internal current and voltage control, a precise bandgap voltage reference and a temperature sensor. The only external signals needed, apart from a power supply, are reference voltages to set the range of the ADC input signal. The developed digitiser comprises also the power-pulsing functionality. About 10 ADC clock periods are needed to restart the correct ADC operation after the pause.
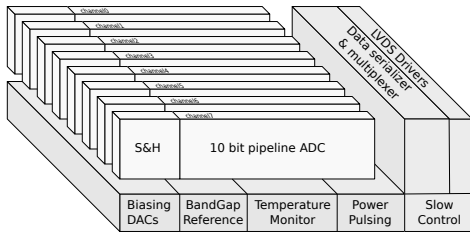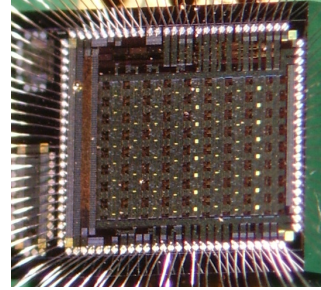
Figure 10: A multichannel ADC block diagram.

Figure 11: A micrograph of ADC ASIC.

A micrograph of the multichannel ADC prototype, glued and bonded on a PCB, is shown in Figure 11. The prototype ASIC was fabricated in 0.35 μm, four-metal two-poly CMOS technology. The active size of the ASIC is 3.17 mm × 2.59 mm. Eight ADC channels are placed in parallel with 200 μm pitch and are followed by the serializer and LVDS pads, while the analog and digital peripheral circuits are on the ASIC sides. The complete measurements of performance, comprising static and dynamic parameters, power consumption, crosstalk, etc., were done and described in detail in [16]. An effective resolution (ENOB) of 9.7 bits was measured in the whole sampling frequency range and for the input frequency up to Nyquist frequency.
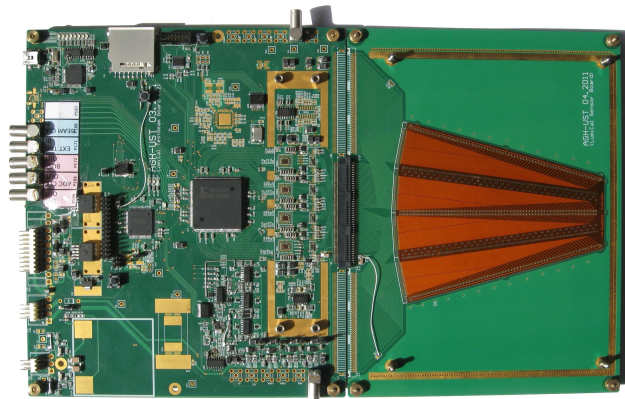
3.3 Detector plane

Figure 12: Photograph of a detector plane with a silicon sensor connected.

A fully assembled detector plane is shown in Figure 12 [17]. In order to increase the system flexibility and to allow the operation with different sensors, the signal is sent to the front-end electronics through a multi-way connector. The signal is then amplified, shaped and continuously digitised. Four pairs of front-end and ADC ASICs, 8 channels each, giving 32 channels in total are placed on the readout board. Power pulsing for the ADC was done by sending a control signal, while for the front-end, additional external switches disconnecting the bias currents were used. To analyse the data, i.e. to reconstruct the signal amplitude and time, and to perform pile-up studies, special attention was given to ensure a sufficiently high ADC sampling-rate and very high internal-data throughput between the ADC and the FPGA. The signal is sampled with a 20 MS/s

rate, and digitised with a 10-bit resolution, resulting in a raw data stream of about 6.4 Gb/s. To fulfill the high throughput requirements, the digital back-end was implemented on a low-cost, high-density Spartan XC3500E FPGA [18] and the ATxmega128A1 microcontroller [19]. The digitised data stream is continuously recorded in a buffer inside the FPGA. When a trigger is received, the acquisition is interrupted and the microcontroller firmware builds an event packet and transmits it to a host PC.The prototype system was fabricated and assembled on a 6-layer PCB.

To verify and to quantify the multichannel readout performance, various laboratory measurements of different system sections and the complete readout chain were done. For the analog part, the measurements of input dynamic range, gain, and noise and their uniformities were performed. For the digital part, the data transmission rate and the event trigger rate in different readout conditions were measured. The performance of the complete readout system in a self-triggering mode was verified with cosmic rays. Additionally, the measurements of power consumption and thermal system behavior in the power-pulsing mode were done. These measurements are described in [17]. After successful completion of the laboratory tests, the developed readout system was used in the beam-tests.

4. Beam-test instrumentation and analysis tools

During 2010 and 2011, the FCAL collaboration performed three beam tests. These were the first tests of the LumiCal silicon- and the BeamCal GaAs-sensors prototypes equipped with a full readout chain. In 2010, the readout comprised a board with two front-end ASICs (16 channels) and an external ADC. In 2011, the complete 32 channel readout module described in Section 3 was used. The detector module performance results include basic signal studies, signal-to-noise measurements, study of tracking with the telescope, response uniformity over the sensor area and shower development measurements with tungsten absorber plates upstream of the sensors.
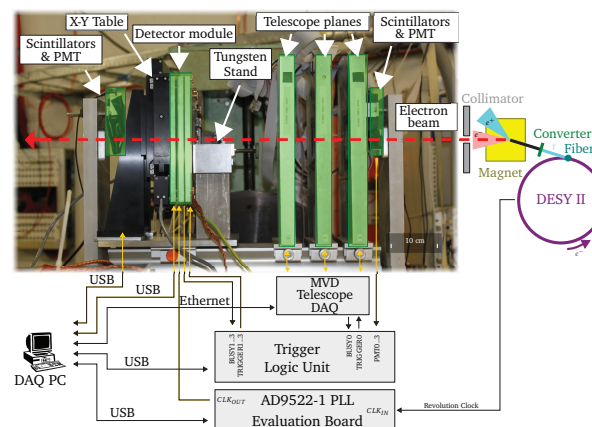
4.1 Beam-tests setup

Figure 13: Scheme of the beam setup from the 2011 test period.

The beam tests were performed at the DESY-II Synchrotron with secondary electrons at different beam-energy. The scheme of the setup for the 2011 test period is shown in Figure 13.

The particles crossed three planes of the ZEUS MVD telescope [20] (MVD). The horizontal and vertical beam size was about 5x5 mm^2. Scintillation counters upstream and downstream of the setup were used in coincidence as trigger counters. In the 2010 tests the sensor was mounted between the second and the third MVD plane inside a shielded PCB box. In 2011, the sensor was installed downstream of the three MVD planes, as shown in Figure 13. The sensor was mounted on a remotely movable X-Y table.

4.2 Telescope

Each plane is made of two 300 μm thick single-sided silicon strip sensors of 32x32 mm^2 size with a strip pitch of 25 μm and a readout pitch of 50 μm. The strip directions of the two sensors in a module are perpendicular to each other. Using the data from each telescope plane, the track of the beam electron can be determined and the point where it hits the device under test (DUT) can be accurately calculated.

A track reconstruction algorithm was developed using the hit-point coordinates for each telescope plane. The distance between the predicted and the measured hit-point coordinates were minimised. The centroids of the clusters of electric charge produced by the passage of incident electrons in the telescope planes were stored. The algorithm used the following condition:

$$min\left(\sum_{i=1}^{3}\left((x_{ip}-x_{im})^2+(y_{ip}-y_{im})^2\right)\right),\qquad(4.1)$$

where (x_{im},y_{im}) are the measured coordinates and (x_{ip},y_{ip}) are the predicted coordinates given by the intersection point of a line with each telescope plane.

Special runs were used to align the MVD planes. The residuals of the intersection point on each telescope plane was determined with an accuracy of about 10 μm, as can be seen in Figures 14(a) and 14(b).
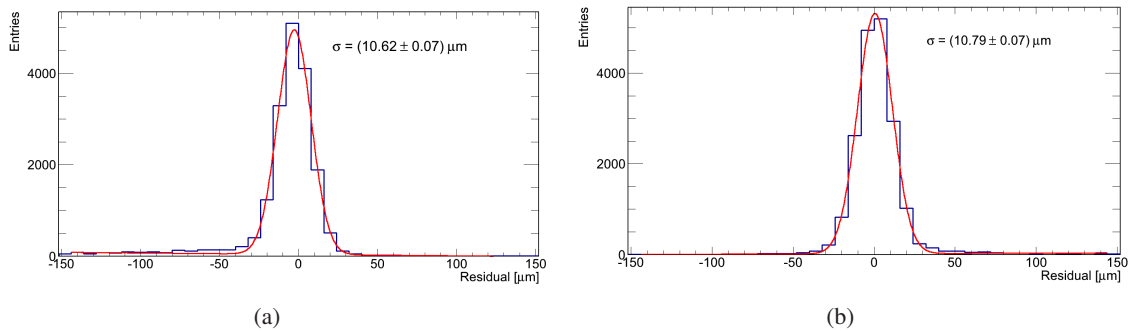

Figure 14: (a) Residual distribution on the X direction. (b) Residual distribution on the Y direction.

After a survey it was still necessary to make some relative shifts between telescope planes, however the shifts were less than 100 μm.

4.3 Data Aquisition System (DAQ)

During the 2010 test the data acquisition system (DAQ) was composed of two separate systems, that of the MVD and that of the detector planes. Each recorded and stored the data independently. A veto scheme was used to ensure that both DAQ systems acquire the same number of events and the event building was done off-line.

For the 2011 tests the EUDAQ [21], a global DAQ software, was used to collect the data from the detectors and to stream simultaneously telescope data to the same file. The trigger logic unit (TLU) [22] was used to generate and distribute a trigger to sub-detectors. Beside acting as a coincidence unit, the TLU provided for each trigger a trigger identification number. This number was used during the data analysis to synchronize between events in a robust way.

To enable the detector-module testing in both synchronous and asynchronous operation modes, the beam revolution clock was delivered from the accelerator to the test setup to synchronise it with the ADC clock.

4.4 Deconvolution

In the setup with the full readout chain, comprising ADC, the pulses were sampled continuously with a frequency of about 20 MHz, asynchronously to the beam, recording 32 samples per channel on the readout board. When the trigger arrived, the acquisition was stopped and a file with 32 samples per each channel was recorded. From the recorded samples, amplitude and time information were reconstructed using a deconvolution procedure outlined below.

The pulse shape at the front-end electronics output is a convolution of the sensor signal and the front-end response. Digitising the output pulse with a continously running ADC and using the known pulse response of the front-end, one can apply a transformation, hereafter referred to as deconvolution, to recover precise time and amplitude of the sensor signal.

The pulse at the front-end electronics output is a convolution of the sensor signal and the front-end response. Sampling and digitising the pulse with a continuously running ADC and taking advantage of a known pulse shape one can perform the inverted procedure, deconvolution, to get the information about the time and the amplitude of the pulse.

The deconvolution idea was proposed for use in pulse shaping in high-energy physics experiments at the beginning of the 90's [23]. It was then implemented in different versions of Analog Pipeline Voltage (APV) ASICs designed for experiments synchronous with beams like CMS at LHC, where the deconvolution was performed by an analog pulse-shape processor (APSP) [24]. The deconvolution principle can be also succesfully used in asynchronous systems to obtain precise timing information in a few ns range, in addition to good signal to noise ratio (SNR) and pileup rejection [25].

For a unit impulse input in a sensor, a semi-Gaussian response $V_{sh}(s) = \frac{1}{(s+1/\tau)^2}$, with time constant τ, is obtained at the output of a CR-RC shaper. To reconstruct the original sensor signal, a deconvolution filter with a transfer function,

$$D(s) = \frac{1}{V_{sh}(s)} = (s+1/\tau)^2, \tag{4.2}$$

is applied. The discrete time implementation of such a filter in a digital domain may be obtained using the Z transform. Using the pole-zero mapping, each pole or zero (on the S plane) is replaced

by its mapped z position according to $z = e^{sT_{smp}}$, where T_{smp} is the sampling period. The formula (4.2) transforms to

$$D(z) = 1 - 2e^{-T_{smp}/\tau} \, z^{-1} + e^{-2T_{smp}/\tau} \, z^{-2}, \qquad (4.3)$$

where z^{-1} is a unit delay. From Eq.(4.3), the expression for deconvolution filtering in a time domain is obtained as

$$d(t_i) = Z^{-1}(D(z)) = V_{sh}(t_i) - 2e^{-T_{smp}/\tau} V_{sh}(t_{i-1}) + e^{-2T_{smp}/\tau} V_{sh}(t_{i-2}). \qquad (4.4)$$

It may be noticed that the deconvolution filter is very light, requiring only two multiplications and three additions.

In Figure 15, an example of the deconvolution filter response to a sampled shaper output is shown. The deconvolution procedure produces only one non-zero sample (Figure 15 (left)) with an
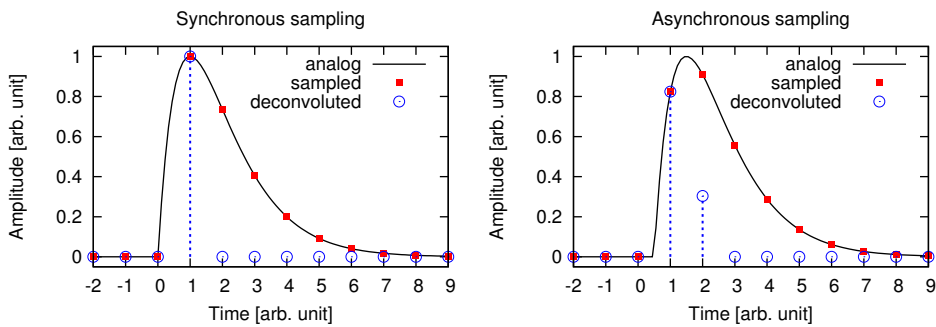
Figure 15: Deconvolution filter response ($T_{smp} = T_{peak} = 1, amp = 1$). Pulse (left) synchronous and (right) asynchronous with the sampling clock.

amplitude proportional to the input pulse. This is the case only when the input pulse is synchronised with the sampling clock. In any other case, the filter produces two non-zero samples (Figure 15 right). The ratio of these samples depends on the phase difference between the input pulse and the sampling clock. Since this ratio is a monotonic function of the phase shift, it can be used to determine the arrival time of the input pulse. The amplitude of the input pulse is obtained from the sum of two non-zero samples multiplied by a time-depended correction-factor. All these operations can be done using look-up tables, possibly offline.

5. Beam-test results

In 2010, several million triggers have been recorded for two sensor areas, on either a LumiCal or a BeamCal detector plane equipped with sensor and front-end ASICs. In 2011, a similar number of triggers have been recorded on a complete detector plane equipped with sensor, front-end ASIC, ADC ASIC, and FPGA-based back-end.

5.1 Study of a detector plane with a silicon sensor

During the 2010 beam test the analog signals were digitised by an external 14-bit ADC (CAEN V1724) with 100 MS/s. The digitised waveforms of 4 channels readout in parallel are shown in Figure 16 [11].
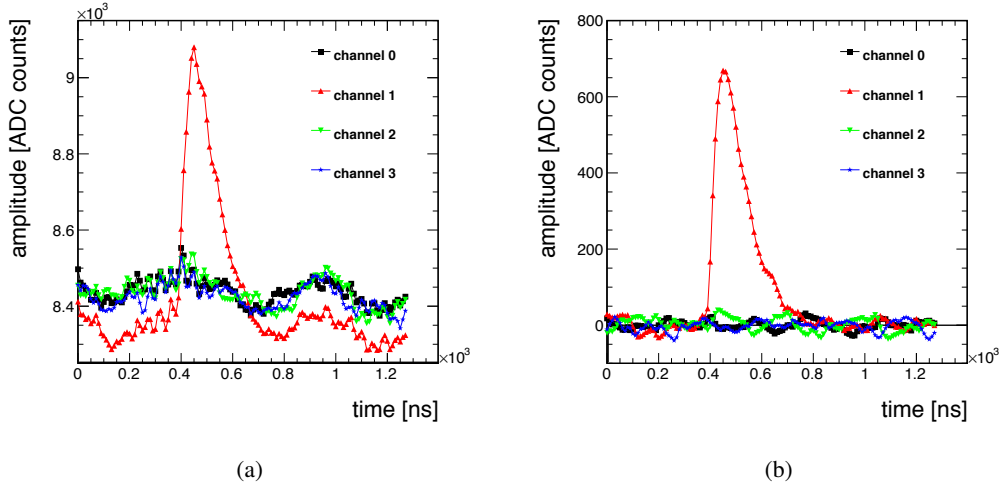
Figure 16: The digitised waveforms of 4 channels, (a) before and (b) after CMN subtraction.

Common Mode Noise (CMN) is determined and subtracted from the raw data, taking into account the different front-end gain for the channels with *MOS* and R_f feedback.

5.1.1 Amplitude spectrum and signal-to-noise ratio

The amplitude is measured with respect to the baseline. Firstly, the average of 32 samples before the arrival of the pulse was used to estimate the baseline mean value, as well as the baseline RMS for each channel, defining the noise. The baseline mean value was subtracted from all samples, shifting the average baseline to zero. The amplitude is obtained as the maximum value of the signal.
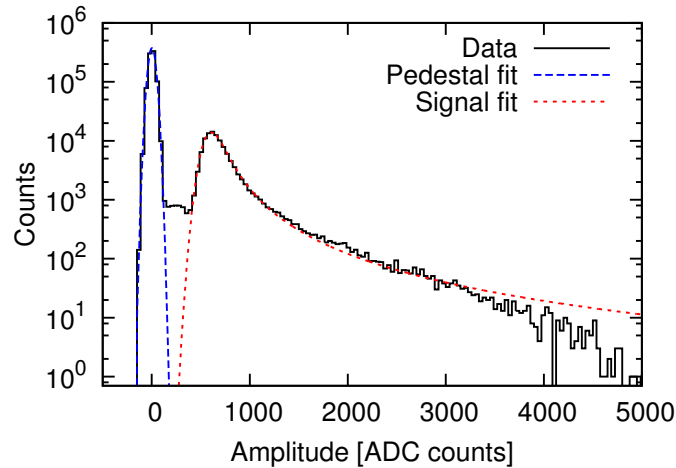
Figure 17: Amplitude spectrum obtained after common mode subtraction and rejection of events with position close to pad borders.

The amplitude spectrum shown in Figure 17 is fit well by a convolution of a Landau distribution and a Gaussian for the signal and a Gaussian for the pedestal. The amplitudes in the pedestal peak are obtained when the acquisition is triggered and no particle is crossing the considered pad. Such a situation is expected to be frequent, having in mind that the beam is collimated to approximately 5×5 mm^2 while the single pad width is only 1.8 mm. Using the most probable value (MPV) and the width of the pedestal, signal-to-noise values between 16 and 22 are measured before the CMN subtraction, and between 28 and 33 after it.

5.1.2 Crosstalk

The relation between signal amplitudes on neighboring pads was studied to evaluate the crosstalk level between pads. Only events identified to lie further than 200 μm from the pad border were used, to minimize the effect of charge sharing. The crosstalk coefficients between all channels are presented in Figure 18(a). One can see a positive correlation between amplitudes of neighboring channels, that can be interpreted as a crosstalk. For the crosstalk measurement, the common mode
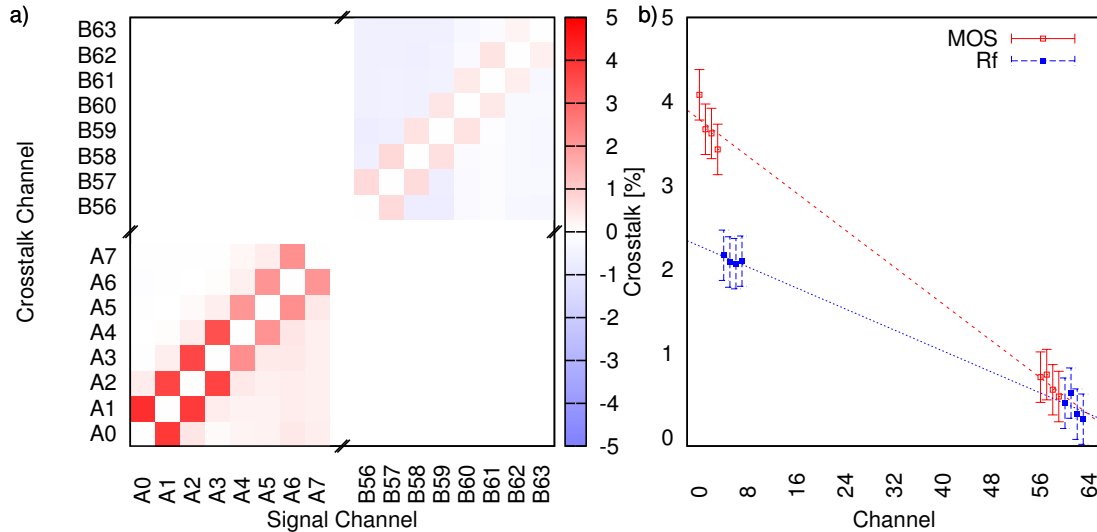

Figure 18: a) Measured crosstalk coefficients for groups of eight pads. b) Measured crosstalk coefficients to the closest neighbor as a function of pad number.

subtraction procedure was not applied to avoid artificially introduced biases. Significant crosstalk can be observed only between the closest neighbors. In Figure 18(b) the estimated crosstalk for pads with long fanout traces (1 - 8) and short fanout traces (56 - 64) is shown. The highest crosstalk is observed for pads with the longest fanout traces (A0 - A7) attached to it. Moreover, there is a significant difference between channels with different feedback type, which can be explained by the differences in the input impedance.

5.1.3 Signal deconvolution

During the beam-test in 2011 the complete readout module with ADC conversion was used. The data were collected in two modes of operation, synchronous and asynchronous with the beam clock.
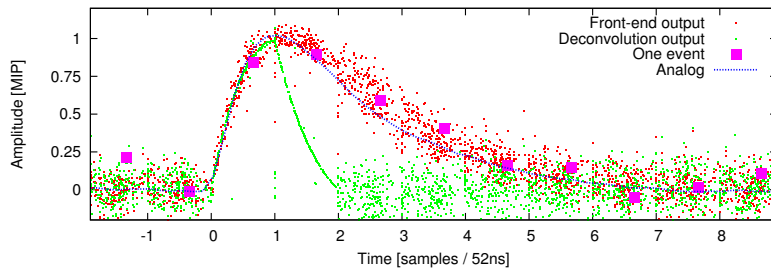
Figure 19: Effect of deconvolution processing (green) on input pulses (red). The pulses were time-aligned using the time information obtained from the deconvolution algorithm. For illustration, an example event is shown as squares.

An example of measured points collected in the asynchronous mode is presented in Figure 19. To extract information about the pulse amplitude and time, the deconvolution method, as described in paragraph 4.4, was used. The waveform, representing an analog output of the front-end electronics captured with a very fast digital oscilloscope, is shown as a reference in red. The events were precisely time-aligned using the information about the time obtained from the deconvolution processing algorithm. The pulse duration after deconvolution is shorter as expected and the amplitude is correctly reconstructed. The signal to noise ratio after deconvolution was similar to the one obtained without deconvolution, running the system in synchronous way.

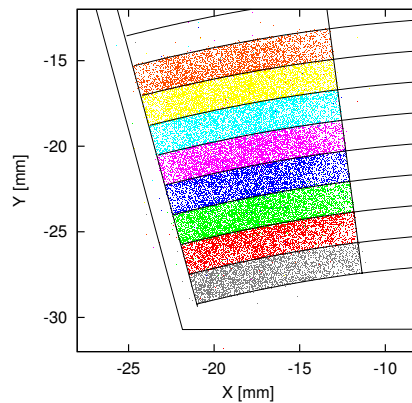### 5.1.4 Response as a function of the position on the sensor

Figure 20: Reconstructed position of impact point on the sensor with color assignment corresponding to the pad with hits above threshold, registered in the LumiCal.

Using a track fit from the MVD telescope, the impact position of the beam electron on the sensor is calculated. The distribution of hits is shown in Figure 20. The colors, characterising the pads, are assigned to each point in case the signal in the pad is above a certain threshold. The pad structure for the LumiCal sensor is correctly reproduced.

In Figure 21 the average amplitude is shown as a function of the position across two adjecent pads. In between the pads a drop of about $\sim 10\%$ is observed in the the $100\,\mu$m gap between pads.
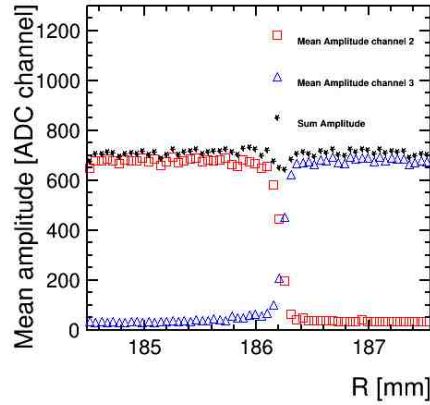

Figure 21: The mean of the signal amplitude as a function of the hit position on the border between two adjecent pads. The star points represent the sum signal of the two neighboring pads for each strip.

5.1.5 Shower development

Using the electron beam, the shower development as a function of the depth of absorber in front of the sensor plane was measured. Because of the stochastic character of the electromagnetic shower development, and having one sensor layer, only average quantities were analysed. For these studies, the electron beam was directed to the center of the instrumented area of the sensor plane. For each absorber thickness, a MC simulation using the GEANT4 framework was done. The electron beam was modeled as isotropically distributed electrons with parallel tracks collimated into a square shape corresponding to the size of the trigger scintillator counters.

Tungsten absorber plates of 3.5 mm thickness, corresponding roughly to one radiation length each, were positioned in front of the sensor plane. For each configuration, 50.000 events were collected and analysed.

The average energy deposited in the instrumented area as a function of the tungsten plate thickness is shown in Figure 22 [26]. The result of the MC simulation is in good agreement with
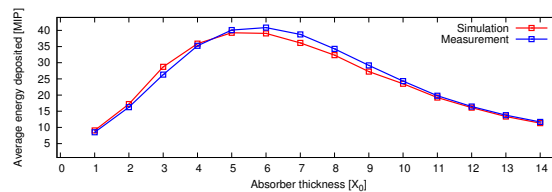

Figure 22: Average energy deposited in the instrumented area as a function of the tungsten absorber thickness, expressed in radiation lengths.

the measurement. The measured shower maximum is observed after six radiation lengths.

5.2 Study of a detector plane with a GaAs sensor

The beam-test data in 2010 were taken using a GaAs pad sensor, FE ASICs and an external 8-bit flash ADC V1721 performing at 500 MS/s. An example of a signal is shown in Figure 23. For each
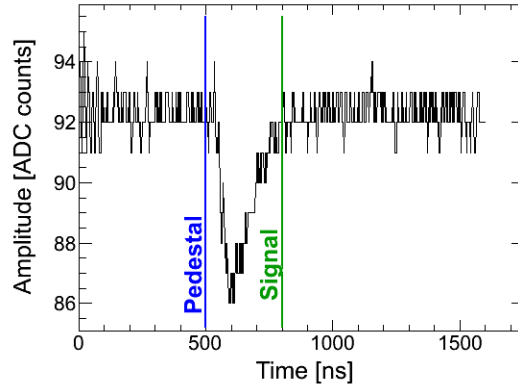

Figure 23: A digitised signal of one channel recorded with a 500 Ms/s ADC.

trigger the signal is digitised in a time window of 1.5 μs. In the first 500 ns, the average baseline and its RMS were evaluated. The adjacent time window of 300 ns is used to analyse the signal. During the 2011 beam test, the signal was split after the FE ASIC and simultaneously digitised by the external ADC (8-bit) and the ADC ASIC (10-bit) on the readout board. Both results are shown in Figure 24, and found to be of the same shape. The raw signal shapes of four adjacent channels of an ASIC are shown in Figure 25. Small common-mode noise is observed which is subtracted from all raw data, taking into account different gains in the channels.
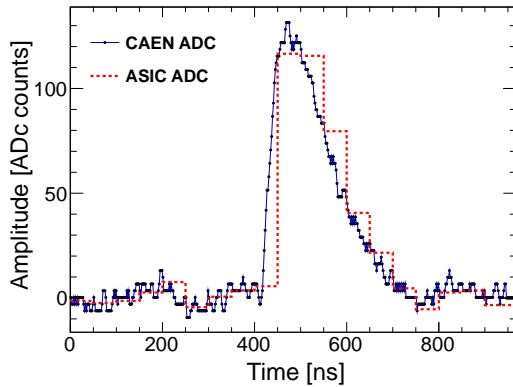

Figure 24: An example of the signal digitised by the external ADC (full line) and the ADC ASIC (dotted line).
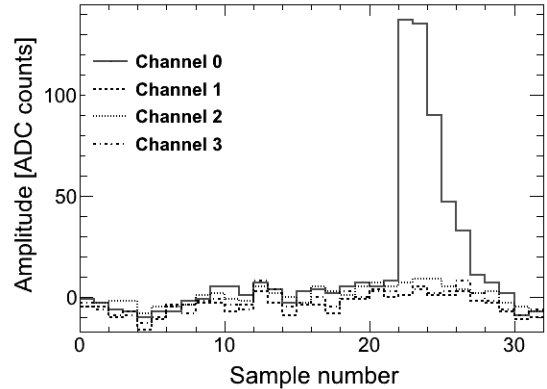

Figure 25: Raw signal shapes of four adjacent channels.

5.2.1 Amplitude spectrum and signal-to-noise ratio

The signal amplitude is defined as the difference between the maximum ADC value in the signal

time window, as shown in Figure 23, and the average baseline. As an example, an amplitude spectrum is shown in Figure 26 for a bias voltage of 100 V. The distributions of the amplitude at
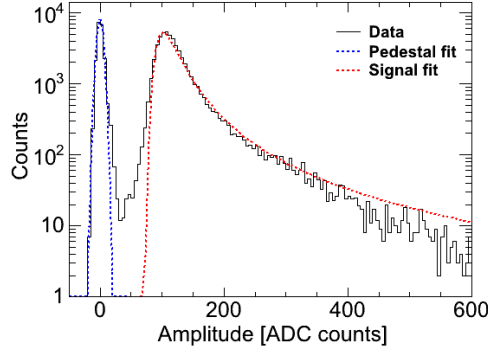

Figure 26: The amplitude spectrum at a bias voltage of 100 V.

each value of the bias voltage are fitted with a convolution of a Gaussian and a Landau distribution to determine the most probable value, MPV. Figure 27 shows the MPV values as a function of the bias voltage for both feed-back types used in the FE ASICs. The MPV grows slowly with increasing voltage and reaches saturation above 60 V. The values of the MPV are transformed into the signal charge using calibration factors obtained by feeding a known charge into the FE ASIC. The deposited charge is obtained from simulations of the energy loss of beam electrons in the sensor, and the energy needed to create an electron-hole pair in GaAs. The charge collection efficiency, defined as the ratio between the signal charge and the deposited charge, approaches 42.2 % at 100 V bias voltage, being in agreement with measurements done in the laboratory [27].
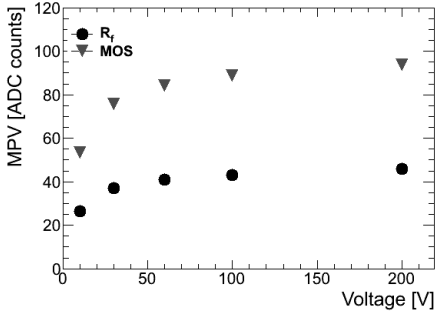

Figure 27: The signal amplitude as a function of the applied bias voltage measured using FE ASICs with R_f and *MOS* feedback.
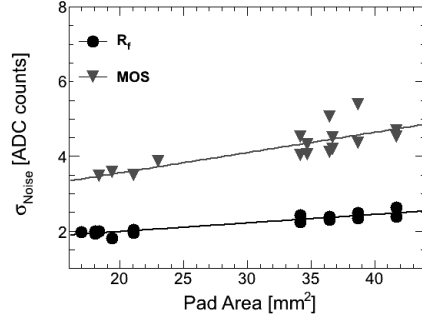
Figure 28: The pedestal standard deviation as a function of the pad area for R_f and *MOS* feedback.

The signal-to-noise ratio was measured using the MPV values and the standard deviation of the pedestal distributions. As an example, the sigma of the pedestal is shown using the amplitude from the 32 readout pads in Figure 28 as a function of the pad size. As can be seen, the noise depends, as expected, almost linearly on the pad size for both front-end feedback types. The values for the R_f feedback are about half the values for the *MOS* feedback.

Using the MPV values of the amplitude distribution, the signal-to-noise values are determined for all channels as

$$S/N = \frac{MPV}{\sigma(Pedestal)}, \tag{5.1}$$

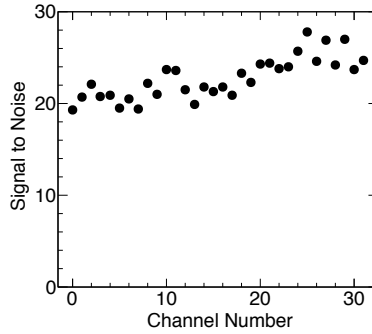and are shown in Figure 29. The slight slope is due to the larger pad areas at low channel numbers.

Figure 29: The signal-to-noise ratios, as a function of the channel number.

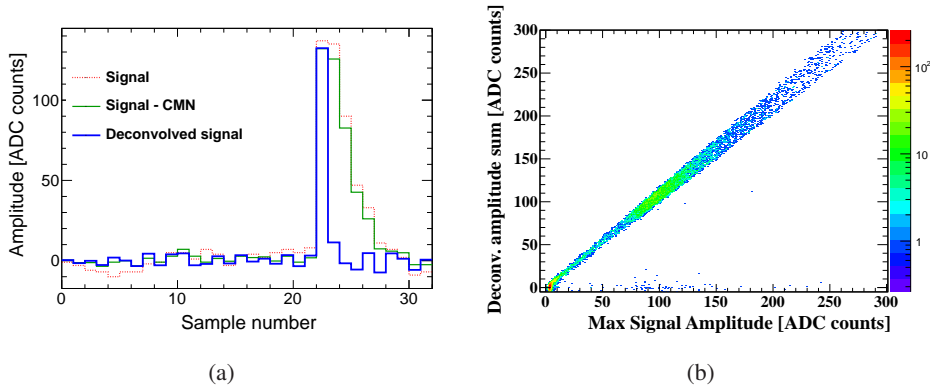### 5.2.2 Signal deconvolution

| (a) | (b) |

Figure 30: (a) The amplitude in channel 0 digitised by the ADC ASICs as a function of time (red), the amplitude values after the common-mode-noise subtraction (green), the deconvoluted amplitude (blue). (b) The sum of two first non zero amplitudes after the deconvolution filter, as a function of the signal amplitude.

Similarly to section 4.4, data were collected in two modes to test the deconvolution method. Figure 30(a) shows the raw signal, the raw signal after CMN subtraction and the deconvoluted signal. For the GaAs data, the time constant is $\tau = 60$ ns and the sampling interval of the ADC Δt=50 ns were used. The pulse after deconvolution is significantly shorter.

Figure 30(b) shows the correlation between the amplitude measured with the ADC and the amplitude obtained after deconvolution in the synchnonous mode. A perfect linear dependence is observed. For the asynchronous operation mode the sum of two non-zero deconvoluted amplitudes shows the same linear dependence with a slightly larger spread [27].

5.2.3 Response as a function of the position on the sensor

Using the MVD telescope, the impact point of each beam electron on the detector plane is calculated. In case the signal of the corresponding pad is above a certain threshold, a pad-depending color is assigned to the impact point. An example distribution of impact points is shown in Figure 31. The pad structure of the GaAs BeamCal sensor is accurately reproduced in the plot. From
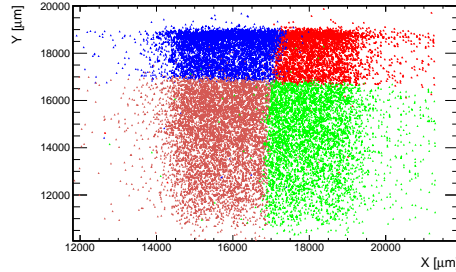

Figure 31: Distribution of the impact points of beam electrons on the GaAs detector plane. A certain color is assigned to each impact point if the signal in the predicted pad is above a certain threshold. The colors are for pads which are numbered in Fig. 4, as follows: pads 2 (red), 5 (green), 6 (blue) and 9 (brown).

amplitude spectra for different areas on the pad the MPVs are determined and found to be in agreement within their statistical uncertainties. The MPVs are also measured in slices of 200 μm covering the non-metallised gap between two pads. For beam electrons with impact points near and in the gap, sharing of the signal between the adjacent pads is observed, as can be see in Figure 32. When the amplitudes on the two adjacend pads are added, their MPV as a function of the position
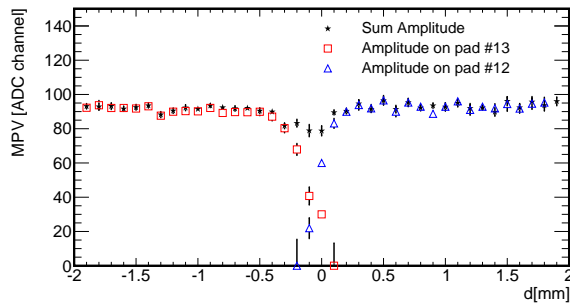

Figure 32: The MPV of the signal amplitude as a function of the hit position on the border between two adjacent pads. The star points represent the sum signal of the two neighboring pads for each strip.

exhibits a drop of about 10% in the region of the gap.

6. Conclusions

Detector plane prototypes for LumiCal and BeamCal were prepared and tested in an electron beam with energies between 2 and 5 GeV. The detector planes comprised silicon or GaAs pad sensors, FE ASICs, ADC ASICs and an FPGA for orchestrating the readout. For both detectors, signal-to-noise

ratios between 20 and 30 are obtained. The performance of FE ASICs with R_f and *MOS* feedback is very similar. A deconvolution method was applied to reduce the amount of recorded data keeping the timing and amplitude information of signals. From studies of the detector response as a function of the beam-electron impact point, a uniform performance was found apart of a reduction of the amplitude of about 10% around the gaps between adjacent pads. A Monte-Carlo simulation of the shower shape as a function of the absorber depth shows good agreement with the measurements. The measured sensor and read-out electronics parameters match the design requirements for the very forward calorimeters at a future linear e^+e^- collider.

Acknowledgments

References

[1] The ATLAS Collaboration, *Observation of a new particle in the search for the Standard Model Higgs boson with the ATLAS detector at the LHC*, Phys.Lett. **B 716** (2012) 1;
The CMS Collaboration, *Observation of a new boson at a mass of 125 GeV with the CMS experiment at the LHC*, Phys. Lett. **B 716** (2012) 30.

[2] T. Behnke, J.E. Brau, B. Foster, J. Fuster, M. Harrison, J.McE. Paterson, M. Peskin, M. Stanitzki, N. Walker, H. Yamamoto (eds), *The International Linear Collider, Technical Design Report*, arXiv:1306.6327.

[3] P. Lebrun, L. Linssen, A. Lucaci-Timoce, D. Schulte, F. Simon, S. Stapnes, N. Toge, H. Weerts, J. Wells (eds), *The CLIC Programme: Towards a Staged e+e- Linear Collider Exploring the Terascale: CLIC Conceptual Design Report*, arXiv:1209.2543.

[4] T. Abe et al., *The International Large Detector: Letter of Intent*, 2010, arXiv:1006.3396.

[5] H. Aihara et al., *SiD Letter of Intent*, 2009, arXiv:0911.0006.

[6] L. Linssen, A. Miyamoto, M. Stanitzki, H. Weerts(eds.), *CLIC Conceptual Design Report: Physics and Detectors at CLIC*, arXiv:1202.5940.

[7] H. Abramowicz et al., *Forward Instrumentation for ILC Detectors*, JINST **5** (2010) 12002.

[8] Ch. Grah and A. Sapronov, *Beam parameter determination using beamstrahlung photons and incoherent pairs*, JINST **3** (2008) 10004.

[9] P. Bambade, V. Drugakov and W. Lohmann, *The impact of BeamCal performance at different ILC beam parameters and crossing angles on stau searches*, Pramada J. Phys. **69** (2007) 1123.

[10] J. Blocki et al., *Silicon sensors prototype for the LumiCal*, Eudet-Memo-2009-07, 2009, http://www.eudet.org/e26/e28/e42441.

[11] I. Levy, *Detector devlopment for the instruments in the forward region of future linear colliders*, MSc Thesis, Tel Aviv University (2012), CERN-THESIS-2012-346.

[12] K. Afanaciev et al., *Investigation of the Radiation Hardness of GaAs Sensors in an Electron Beam* JINST **7** (2012) 11022.

[13] M. Idzik, H. Henschel, W. Lohmann et al., *Status of VFCAL*, EUDET-memo-2008-01, 2008.

[14] T. Behnke et al. (eds), *The ILC Technical Design Report, Vol 4, Detectors*, June 2013, arXiv:1306.6329.

[15] M. Idzik, Sz. Kulis, D. Przyborowski, *Development of front-end electronics for the luminosity detector at ILC*, Nucl. Inst. Meth. **A 608** (2009) 169.

[16] M. Idzik, K. Swientek, T. Fiutowski, Sz. Kulis, D. Przyborowski, *A 10-bit multichannel digitiser ASIC for detectors in particle physics experiments*, IEEE Trans. Nucl. Sci. **59** (2012) 294.

[17] Sz.Kulis, A. Matoga, M. Idzik, K. Swientek, T. Fiutowski, D. Przyborowski, *A general purpose multichannel readout system for radiation detectors*, JINST **7** (2012) T01004.

[18] *Xilinx Inc.,Spartan-3E FPGA Family Data Sheet*, August 2009., http://www.xilinx.com/support/documentation/data_sheets/ds312.pdf.

[19] *Atmel Corporation, ATxmega64A1/128A1/192A1/256A1/384A1 Preliminary*, September 2010, http://www.atmel.com/dyn/products/product_card.asp?part_id=4298.

[20] *ZEUS MVD Telescope*, http://www.desy.de/g̃regor/short_intro.html.

[21] E. Corrin, *EUDAQ Software User Manual*, EUDET-Memo-2010-01, 2010.

[22] D.G. Cussans, *Description of the JRA1 trigger logic unit (TLU), v0.2c*, EUDETMemo-2009-04, 2009.

[23] T.L. Bienz, *Strangeonium spectroscopy at 11 GeV/c and Cherenkov ring imaging at the SLD*, Ph.D Thesis.

[24] S. Gadomski, G. Hall, T.Hogh, P. Jalocha, E. Nygard, P. Weilhammer, *The deconvolution method of fast pulse shaping at hadron colliders*, Nucl. Instr. Meth. **A 320** (1992) 217.

[25] Sz. Kulis, M. Idzik, *Triggerless readout with time and amplitude reconstruction of event based on deconvolution algorithm*, Acta Physica Polonica B Proceedings Supplement **4** (2011) 49.

[26] Sz. Kulis, *Development of prototype luminosity detector modules for future experiments on linear colliders*, PhD Thesis, AGH University of Science and Technology (2013), CERN-THESIS-2012-358.

[27] O. Novgorodova, *Characterisation and application of radiation hard sensors for LHC and ILC*, PhD Thesis, Cottbus University (2013), DESY-THESIS-2013-052.